Composites: Part A 212 (2027) 110251

Contents lists available at ScienceDirect

Composites Part A

journal homepage: www.elsevier.com/locate/compositesa

$Ti_3C_2T_x$@PANI/shape memory polyimide composites for thermal actuation, electromagnetic shielding, and flame retardancy

Xiaofei Wang [a], Ying Dai [a], Shuting Jiang [b], Xinli Xiao [b], Yanju Liu [c], Jinsong Leng [d,*]

[a] Suzhou Research Institute, Harbin Institute of Technology, Suzhou 215100, PR China
[b] MIIT Key Laboratory of Critical Materials Technology for New Energy Conversion and Storage, School of Chemistry and Chemical Engineering, Harbin Institute of Technology, Harbin 150001, PR China
[c] Department of Astronautical Science and Mechanics, Harbin Institute of Technology, Harbin 150001, PR China
[d] National Key Laboratory of Science and Technology on Advanced Composites in Special Environments, Harbin Institute of Technology, Harbin 150080, PR China

HIGHLIGHTS

- MXene is etched to generate abundant surface groups and intercalated with PANI to form $Ti_3C_2T_x$@PANI.
- $Ti_3C_2T_x$@PANI/SMPI composite achieves EMI shielding efficiency exceeding 28 dB within the X-band range.
- The smart composite exhibits excellent shape memory performance and synergistic flame retardancy.

GRAPHICAL ABSTRACT

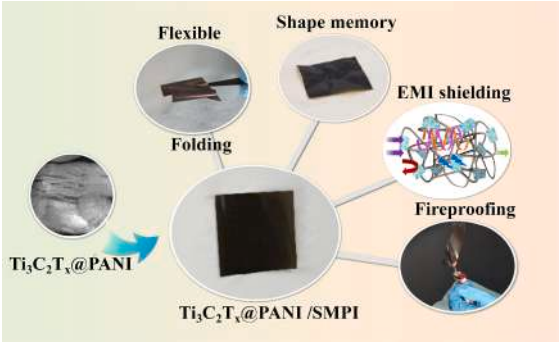

ARTICLE INFO

Keywords:
Shape memory polyimide composite
$Ti_3C_2T_x$@PANI intercalation complex
EMI
Flame retardant

ABSTRACT

Electromagnetic wave pollution poses threats not only to human health, but also to information security and the operational reliability of precision instruments. Therefore, it is essential to effectively protect against electromagnetic waves and suppress electromagnetic wave radiation and interference. Here, a high-temperature intelligent electromagnetic shielding material is designed by integrating shape memory polyimide with a two-dimensional MXene-based intercalation complex. MXene sheet particles were first etched to enrich their surfaces with –OH, =O, –F, and –Cl polar groups. Conductive polyaniline (PANI) was then intercalated into MXene to obtain $Ti_3C_2T_x$@PANI intercalation complexes. The smart composite exhibits high thermal stability, favorable mechanical properties, and excellent flame retardancy. In addition, the electromagnetic shielding efficiency of the smart composite in the X-band exceeds 28 dB, effectively shielding over 99 % of the incident microwaves. It also has excellent shape memory characteristics, with a shape fixation ratio of 96 % and a shape recovery ratio of 97 %. Therefore, it will be applied in cutting-edge technological fields such as electronic appliances, thermal management electromagnetic shielding devices and smart wearable devices.

* Corresponding author.
E-mail address: lengjs@hit.edu.cn (J. Leng).

https://doi.org/10.1016/j.compositesa.2026.110251
Received 13 May 2026; Received in revised form 30 August 2026; Accepted 30 August 2026
Available online 31 August 2026

1. Introduction

After air, water, and noise pollution, electromagnetic pollution has emerged as a significant environmental and public health concern. The release of high-density electromagnetic energy into the environment not only threatens human health but also endangers information security and the operational reliability of precision instruments. Consequently, effective electromagnetic shielding, prevention of electromagnetic information leakage, and suppression of electromagnetic radiation and interference are pressing challenges [1–3]. Conventional metallic shielding materials have limitations in many applications because of their high density, limited flexibility, narrow absorption bandwidth, and poor corrosion resistance. With the growing demand for lightweight, portable, and wearable electronic devices, alternatives to conventional metallic EMI-shielding materials are urgently required [4–6]. A combination of good flexibility, electrical conductivity, and ease of processing makes conductive polymer composites a highly promising candidate for electromagnetic interference (EMI) shielding materials [7,8]. Choi et al. [9] prepared a 43-μm-thick graphene/cellulose composite via spray deposition, which achieved an EMI shielding effectiveness of 28.3 dB at 10 GHz and was therefore suitable for wearable electronics. Bai et al. [10] developed a multifunctional shape memory polyurethane composite that combined EMI shielding, infrared stealth, and intelligent actuation, with tunable EMI shielding effectiveness from 60.0 to 11.0 dB under 0–30 % tensile strain in the X-band. In 2025, Wang et al. [11] reported a shape memory liquid–metal/polyimide/aramid-nanofiber composite aerogel with programmable electromagnetic switching and EMI shielding effectiveness up to 28.21 dB at high strains (50–80 %). These studies indicate that combining EMI shielding with shape memory behavior can produce intelligent, integrated polymer composites and broaden their application scope.

Shape memory polymers (SMPs) can undergo programmed shape changes in response to specific external stimuli, making them promising for deployable space structures, biomedical engineering, tunable flexible electronics, and soft robotics [12–17]. Shape memory polyimide (SMPI) is poised for extensive application in high-end technologies such as flexible electronics and aerospace. This is attributed to its exceptional resistance to both high and low temperatures, coupled with its superior mechanical properties, flexibility, dimensional stability, corrosion resistance, and radiation resistance [18–20]. Liu et al. [21] reported a high-transition-temperature SMPI aerogel composite prepared from polyimide and graphene oxide via freeze-drying and thermal annealing, which exhibited a high transition temperature (280 °C), robust thermomechanical performance, and excellent shape recovery. However, pristine SMPI requires modification for electromagnetic shielding, as its high electrical resistivity and low dielectric constant limit shielding performance. MXenes are two-dimensional transition-metal carbides/nitrides obtained by selectively etching active metal layers from MAX phases, among which $Ti_3C_2T_x$ is the most widely studied. $Ti_3C_2T_x$ surfaces are rich in –OH, =O, and −F functional groups and exhibit high electrical conductivity (up to 2.4×10^4 S/cm), favorable electrochemical properties, and efficient photothermal conversion [22–25]. Duan et al. [26] designed an ultrathin $Ti_3C_2T_x$ film treated with a low-concentration NaOH gradient to regulate hydroxyl groups. $Ti_3C_2T_x$ treated with 0.2 mol/L NaOH showed the highest hydroxyl concentration and achieved a shielding effectiveness of 48.965 dB at a thickness of 0.016 mm. Yan et al. [27] fabricated a flexible hydrophobic polyimide/MXene-POSS nanocomposite film with a shielding effectiveness of 12.7 dB at 20 wt% MXene-POSS loading. Nevertheless, electromagnetic-shielding materials dissipate electromagnetic waves as heat, which may increase device operating temperature. Fire safety is therefore another critical requirement for practical EMI-shielding materials.

In this work, an organic–inorganic hybrid SMPI composite with flame-retardant and EMI-shielding functions was designed by combining a smart polymer matrix with a two-dimensional $Ti_3C_2T_x$@PANI intercalation complex. The MXene intercalation complex acts as a layered reinforcing phase in the SMPI matrix, where rigid $Ti_3C_2T_x$ nanosheets and conductive PANI promote interfacial interactions and stress transfer. Previous studies have shown that ordered rigid nanodomains dispersed in a continuous polymer matrix can effectively improve strength and toughness [28–30]. Song et al. [31] incorporated modified graphene oxide nanosheets with dynamic hydrogen-bonding capability into a polyurethane matrix. The resulting composite contained a dense hydrogen-bonding network and showed a tensile strength of 39.6 MPa, an elongation at break of 1155.6 %, and a self-healing efficiency of 90.3 %. Li et al. [32] constructed a high-performance composite adhesive by functionalizing BN nanosheets with chitosan. Compared with the neat adhesive, the composite adhesive exhibited substantially improved mechanical properties, with dry and wet shear strengths of 1.96 and 1.31 MPa, respectively.

The main innovations of this study are as follows. First, MXene was etched to enrich its surface with –OH, =O, −F, and −Cl polar groups and then intercalated with conductive polyaniline (PANI) to form $Ti_3C_2T_x$@PANI intercalation complexes. The folded lamellar $Ti_3C_2T_x$/PANI architecture served as a reinforcing phase, thereby improving the strength and toughness of the resin matrix. Second, the $Ti_3C_2T_x$/PANI intercalation complex was incorporated into SMPI to obtain composites with high EMI shielding effectiveness and flame retardancy. Third, a synergistic flame-retardant effect was established between the SMPI matrix and $Ti_3C_2T_x$/PANI. During combustion, $Ti_3C_2T_x$ is oxidized in air to generate TiO_2 and carbon. The newly formed TiO_2 creates a physical protective barrier at the MXene-SMPI interface, encapsulating the carbonized SMPI residue and suppressing further combustion and flame propagation. These multifunctional composites are promising for adaptive flexible thermal management, EMI-shielding devices, and smart wearable devices.

2. Experimental section

2.1. Raw materials and reagents

Conductive polyaniline (98 %, conductivity 2 S/cm) was purchased from McLean Reagent Co., Ltd. 4,4′-(Hexafluoroisopropylene)diphthalic anhydride (>99 %, 6FDA) and 4,4′-diaminodiphenyl ether (>99 %, ODA), N, N-dimethylacetamide (DMAc), Ti_3AlC_2 powder (diameter < 30.8 μm), hydrochloric acid (HCl, 37 %), and lithium fluoride (LiF, AR, >99 %) were all sourced from Shanghai Aladdin Reagent Co., Ltd.

2.2. Preparation of shape memory composites $Ti_3C_2T_x$@PANI/SMPI

2.2.1. Preparation of $Ti_3C_2T_x$

First, 1 g of LiF was dissolved in 20 mL of 9 mol/L HCl. The mixture was transferred to an ice-water bath, and 1 g of Ti_3AlC_2 powder was gradually added. After reagent addition, the reaction mixture was maintained at 35 °C for 24 h for etching. The reaction mixture was centrifuged and washed with water until neutral, then ultrasonicated for 1 h to obtain few-layer $Ti_3C_2T_x$. Finally, the suspension was centrifuged at 3500 r/min for 1 h to remove incompletely etched large particles.

2.2.2. Preparation of intercalation compounds $Ti_3C_2T_x$@PANI

A $Ti_3C_2T_x$ sample (0.25 g) was dispersed in 50 mL of DMAc and continuously stirred at 40 °C for 48 h, followed by ultrasonic dispersion for 4 h to obtain a dark suspension with a concentration of 5 mg/mL. Conductive polyaniline powder (0.0125 g) was then added to the suspension, and the mixture was allowed to undergo intercalation for 4 h, yielding a $Ti_3C_2T_x$@PANI intercalation-complex suspension.

2.2.3. Preparation of $Ti_3C_2T_x$@PANI/SMPI

(1) A certain amount of ODA was dissolved in DMAc, followed by the stepwise addition of 6FDA (4–6 times) under a N_2 atmosphere. The mixture was stirred at 200–300 r/min for 20 h at room

temperature, and a content of 17 wt% polyamic acid (PAA) solution was obtained. Among them, the molar ratio of ODA to 6FDA was maintained at 1:1.

(2) A predetermined amount of $Ti_3C_2T_x$@PANI intercalation composite suspension was blended with the PAA solution and subjected to stirring at 500 r/min for 4 h for complete mixing. The resulting mixture was then transferred onto a glass plate. A series of mixtures were prepared with $Ti_3C_2T_x$@PANI loadings of 2, 4, 6, 8, and 10 wt% relative to the mass of PAA.

(3) The imidization was conducted through a stepwise temperature increase, yielding shape memory polyimide composites that exhibited electromagnetic shielding, flame retardancy, and shape memory properties. The material was heated in a stepwise manner to successively higher temperatures: 50, 80, 120, 160, 200, 250, and 300 °C. The corresponding dwelling times were 5, 5, 2, 2, 2, 2, and 2 h at each temperature. They were named $Ti_3C_2T_x$@PANI/SMPI-2, $Ti_3C_2T_x$@PANI/SMPI-4, $Ti_3C_2T_x$@PANI/SMPI-6, $Ti_3C_2T_x$@PANI/SMPI-8, and $Ti_3C_2T_x$@PANI/SMPI-10, respectively. A schematic of the preparation process is presented in Fig. 1.

2.3. Characterization

Structural characterization: Fourier transform infrared (FTIR) was performed using the AVATAR360 spectrometer on Ti_3AlC_2, $Ti_3C_2T_x$, $Ti_3C_2T_x$@PANI intercalation complex, and $Ti_3C_2T_x$@PANI/SMPI composites. The test range was 4000–500 cm^{-1}. The KBr pellet method was used for Ti_3AlC_2, $Ti_3C_2T_x$, and $Ti_3C_2T_x$@PANI intercalation complex, while the ATR method was employed for $Ti_3C_2T_x$@PANI/SMPI composites. To monitor the etching and intercalation reactions, wide-angle X-ray diffraction (WAXD) was performed on Ti_3AlC_2, $Ti_3C_2T_x$, and $Ti_3C_2T_x$@PANI. Furthermore, the technique was used to evaluate the crystallinity of SMPI composites incorporating varying amounts of $Ti_3C_2T_x$@PANI, with all scans conducted over a 2θ range of 0° to 80°.

Morphology and elemental analysis: The microstructure and dimensions of the etched MXene sheets were analyzed by scanning electron microscopy-energy dispersive X-ray spectroscopy (SEM-EDS) and high-resolution transmission electron microscopy (HRTEM). The resolution was 0.23 nm and the magnification was 350,000 times. The lateral size and thickness of the etched MXene sheets were determined by atomic force microscopy (AFM). Cross-sectional microstructures of the $Ti_3C_2T_x$@PANI/SMPI samples were characterized by SEM at different magnifications; prior to imaging, the samples were sputter-coated with gold for 30 s, and observations were performed at an accelerating voltage of 5 kV.

Thermal and mechanical characterization: The dynamic mechanical properties of the $Ti_3C_2T_x$@PANI/SMPI composites were measured using a DMA Q800 dynamic mechanical analyzer (TA Instruments, USA). Measurements were conducted under a nitrogen purge of 10.00 mL/min over 25–500 °C at a heating/cooling rate of 5 °C/min, with an amplitude of 0.2 % and a frequency of 1 Hz. Thermogravimetric analysis (TGA) of the $Ti_3C_2T_x$@PANI/SMPI composites was performed using a TGA/DSC1 simultaneous thermal analyzer (METTLER TOLEDO, Switzerland). The tests were conducted from 25 to 800 °C at a heating rate of 10 °C/min under N_2, with sample masses of 5–10 mg. Composite films were prepared according to GB13022-91. Mechanical properties were measured using an SBA-10 tensile testing machine (Chongqing Hake Technology Co., Ltd.) at a constant loading speed of 5 mm/min. Five tensile tests were performed for each composition, and tensile strength, Young's modulus, and elongation at break were reported as average values. The plotted values are presented as mean ± standard deviation.

Electromagnetic shielding and environmental-resistance tests: Electromagnetic interference (EMI) shielding effectiveness was measured using a Keysight N5222B vector network analyzer (VNA) via the waveguide method. The scattering parameters (S11 and S21) were first recorded across the X-band (8.2–12.4 GHz). These parameters were then used in Eqs. (1–6) to derive the transmission (T), reflection (R), and absorption (A) coefficients. Subsequently, the total shielding effectiveness (SE_T) and its components from reflection (SE_R) and absorption (SE_A) were obtained.

$$R = |S_{11}|^2 \tag{1}$$

$$T = |S_{21}|^2 \tag{2}$$

$$A = 1 - R - T \tag{3}$$

$$SE_R = -10log(1-R) \tag{4}$$

$$SE_A = -10log[T/(1-R)] \tag{5}$$

$$SE_T = SE_R + SE_A \tag{6}$$

Extreme environment tolerance tests: To evaluate the EMI shielding stability of the $Ti_3C_2T_x$@PANI/SMPI composites, samples were subjected to 100 bending cycles, ultrasonic treatment for 30 min, immersion in liquid nitrogen (−196 °C) for 30 min, and heat treatment at 150 °C. Chemical resistance was evaluated by immersing the composites

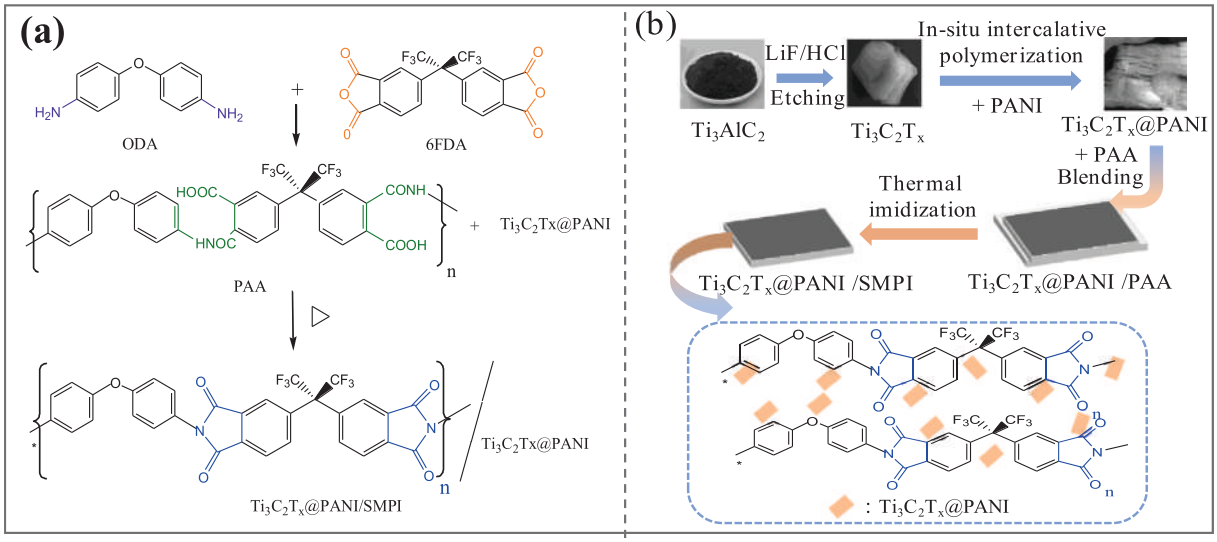

Fig. 1. (a) The preparation route of $Ti_3C_2T_x$@PANI/SMPI composites, (b) Schematic diagram of the preparation process for $Ti_3C_2T_x$@PANI/SMPI composite.

separately in acidic and alkaline solutions with pH values of 1 and 14 for 30 min.

Flame retardancy tests: The vertical burning test of the $Ti_3C_2T_x$@-PANI/SMPI composite was performed according to GB/T 2409–84 to evaluate flame retardancy. SEM-EDS was used to characterize the microstructure and elemental composition of samples after combustion. The flame retardancy grade was evaluated according to UL94-2009. The limiting oxygen index (LOI) was measured using a ZY6155 oxygen index tester (Taiwan Songshu Co., Ltd.) according to ISO 4589–2. The sample size was 120 mm × 10 mm, 8–10 specimens were tested, and the O_2 concentration was increased from 25 % until the specimen burned.

Shape memory performance test: (1) The qualitative test was performed as follows: The $Ti_3C_2T_x$@PANI/SMPI sample was programmed by heating it to $T_g + 10$ °C, maintaining this temperature for 5 min, and then deforming it into a "U"-shape with a 2.5 mm radius of curvature by applying an external force. The sample was clamped in the deformed "U" shape at 25 °C. After the external force was released and the sample was held for 5 min, the temporary shape was fixed. The sample was then reheated to $T_g + 10$ °C to trigger shape recovery. (2) DMA was used to quantitatively evaluate the shape memory performance. In an N_2 atmosphere, the sample was heated to $T_g + 10$ °C at a rate of 10 °C/min, at which point the sample was stretched from ε_0 to $\varepsilon_0 + \Delta L$ at a strain ratio of 5 %. Cooling to 220 °C at 10 °C/min was performed under constant applied stress, at which point the loaded stress was removed and the strain $\varepsilon_0 + \Delta L'$ was recorded. Finally, the sample was reheated to $T_g + 10$ °C to obtain the recovered strain ε_{rec}. The shape fixation ratio (R_f) and shape recovery ratio (R_r) of $Ti_3C_2T_x$@PANI/SMPI composites were calculated using Eqs. (7) and (8), respectively.

$$R_f = (\varepsilon_0 + \Delta L')/(\varepsilon_0 + \Delta L) \times 100\% \quad (7)$$

$$R_r = \varepsilon_{rec}/(\varepsilon_0 + \Delta L') \times 100\% \quad (8)$$

In Eq. (7) and Eq. (8), $\varepsilon_0 + \Delta L$ was the maximum strain value under stress (mm).

$\varepsilon_0 + \Delta L'$ was the fixed strain value after removing external force (mm).

ε_{rec} was the recovery value of the strain after heating (mm).

3. Results and discussion

3.1. Molecular structure and aggregate state structure

FTIR spectroscopy was used to compare the functional-group features of PANI, $Ti_3C_2T_x$, and $Ti_3C_2T_x$@PANI in Fig. 2(a). The broad bands centered at 3132 and 3160 cm^{-1} in $Ti_3C_2T_x$ and $Ti_3C_2T_x$@PANI, respectively, are mainly attributed to O–H stretching from surface hydroxyl groups and adsorbed water; N–H stretching from PANI may also contribute to the composite band. The features in the 1700–1600 cm^{-1} region comprise overlapping contributions from oxygen-containing surface species and adsorbed water in $Ti_3C_2T_x$ and the quinoid-ring C=C/C=N vibrations of PANI. For $Ti_3C_2T_x$, the bands at 1143 and 937 cm^{-1} are consistent with vibrations associated with surface −F/-O terminations and Ti-O bonds, while the band at 556 cm^{-1} is assigned to Ti-O/Ti-OH-related vibrations. For PANI, the bands at 1614 and 1465 cm^{-1} are assigned to quinoid- and benzenoid-ring stretching, respectively, and the band at 1114 cm^{-1} is associated with C–H in-plane bending in protonated PANI. In the $Ti_3C_2T_x$@PANI spectrum, the features at 1605, 1466, and 1111 cm^{-1} are consistent with PANI-related vibrations and overlap with contributions from $Ti_3C_2T_x$. Because a weak feature near 1465 cm^{-1} is also visible in the red $Ti_3C_2T_x$ spectrum, this band is not used alone to prove PANI incorporation. Rather, the simultaneous presence and overall combination of the PANI-related features with the $Ti_3C_2T_x$-related features support the formation of the $Ti_3C_2T_x$@PANI hybrid.

In addition, the crystal structures of Ti_3AlC_2, $Ti_3C_2T_x$ and $Ti_3C_2T_x$@PANI were analyzed by WAXD. In Fig. 2(b), compared with Ti_3AlC_2, the acid-etched MXene sample $Ti_3C_2T_x$ broadened and shifted toward lower angles at (002), (004), (101) and (105). The characteristic Al (104) peak at 39° weakened, with only a slight peak, indicating that the Al atoms in $Ti_3C_2T_x$ were effectively removed. In addition, the (002)

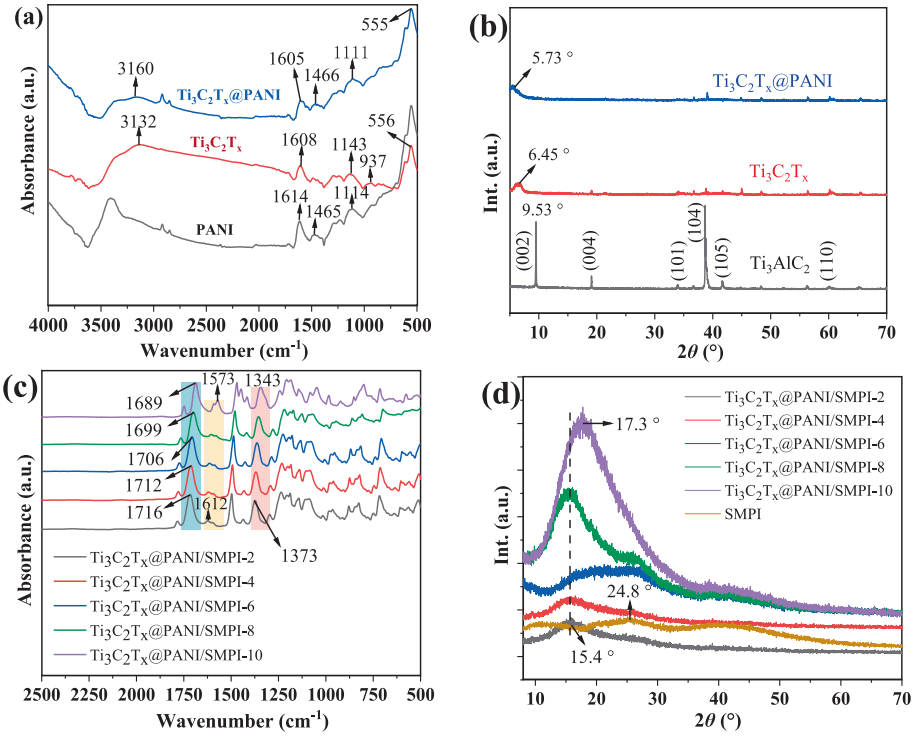

Fig. 2. (a) The FTIR spectrum of Ti_3AlC_2, $Ti_3C_2T_x$ and $Ti_3C_2T_x$@PANI, (b) The WAXD spectrum of Ti_3AlC_2, $Ti_3C_2T_x$ and $Ti_3C_2T_x$@PANI, (c) The FTIR spectrum of $Ti_3C_2T_x$@PANI/SMPI composites, (d) The WAXD spectrum of $Ti_3C_2T_x$@PANI/SMPI composites and SMPI.

peak shifted from 9.53° to 6.45°, and according to Bragg's equation $n\lambda = 2dsin\theta$, the interlayer spacing of etched $Ti_3C_2T_x$ increased. Furthermore, the (002) peak at 5.73° was observed in the spectrum of the $Ti_3C_2T_x$@PANI intercalation complex, indicating that PANI acted as an intercalant and expanded the $Ti_3C_2T_x$ interlayer spacing.

FTIR was used to characterize the molecular structures of $Ti_3C_2T_x$@PANI/SMPI composites with different MXene loadings. As shown in Fig. 2(c), the absorptions at 1343–1373 and 1689–1716 cm^{-1} were assigned to C-N and symmetric C=O stretching vibrations, respectively, both of which are characteristic of the polyimide structures. Completion of imidization was confirmed by the appearance of characteristic imide bands and the disappearance or marked weakening of amic-acid-related bands. As the $Ti_3C_2T_x$@PANI intercalation-complex content increased, both bands shifted to lower wavenumbers. This red shift is attributed to interfacial interactions among surface functional groups on $Ti_3C_2T_x$ (–OH, =O, and −F), PANI chains, and the SMPI matrix. The abundant polar groups on MXene can form intermolecular hydrogen bonds with the imide groups (–CO-N-CO-) of SMPI. Together with possible dipole–dipole and π-π stacking interactions among MXene, PANI, and SMPI, these interactions reduce the local electron density of the C=O and C-N bonds in the imide rings and decrease their bond force constants. According to Hooke's law, the decrease in force constant lowers the vibrational frequency, which appears as a red shift in the FTIR spectra. In addition, the peak at 1612–1573 cm^{-1} was assigned to C=C stretching vibrations of benzenoid or quinoid rings in PANI.

WAXD was used to characterize the aggregate structure of the synthesized SMPI and $Ti_3C_2T_x$@PANI/SMPI composites. In Fig. 2(d), the neat SMPI exhibits a broad amorphous diffraction peak, at $2\theta = 24.8°$. This broad peak indicates that the films were mainly amorphous, with partial ordered chain packing. This phenomenon also indirectly confirmed that the shape memory switching transition of the material was its glass transition, rather than a crystalline melting point. Upon incorporation of $Ti_3C_2T_x$@PANI nanosheets, this amorphous peak shifts toward lower 2θ values, and a new broad amorphous halo emerges within the 2θ range of 15.4°–17.3° for composite films. According to the Bragg equation $n\lambda = 2dsin\theta$, d is inversely proportional to $sin\theta$. With increasing $Ti_3C_2T_x$@PANI intercalation-complex content, the 2θ diffraction angle shifted to higher angles, indicating that the interplanar spacing of the polymer decreased. These results indicate denser packing, stronger intermolecular interactions, and higher crystallinity. This behavior is related to the good flexibility, regular arrangement, and tight packing of SMPI molecular chains. When dispersed within the polymer matrix, the two-dimensional MXene layers served as a template that promoted the regular organization of the molecular chains, thereby

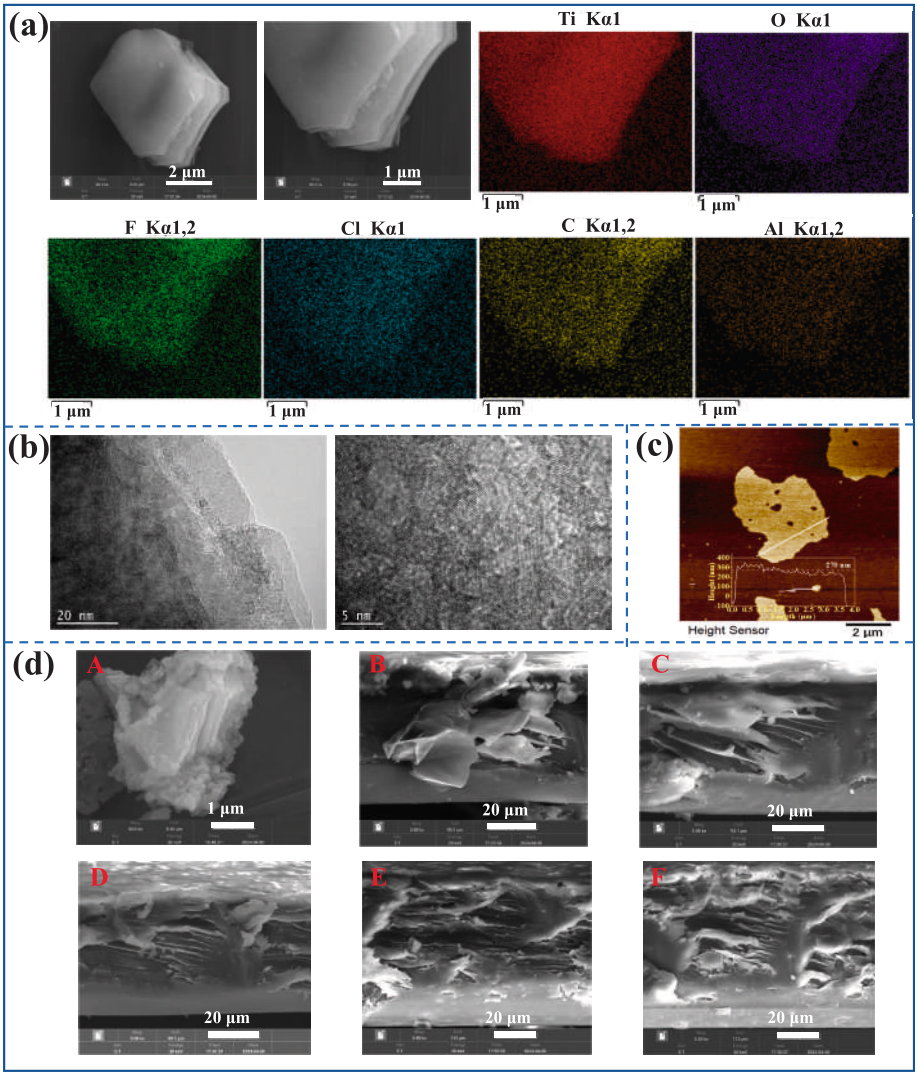

Fig. 3. (a) The SEM-EDS images of MXene, (b) The HRTEM images of MXene, (c) The AFM images of MXene, (d) The SEM images of $Ti_3C_2T_x$@PANI and $Ti_3C_2T_x$@PANI/SMPI composites, specifically, A was the $Ti_3C_2T_x$@PANI, B to F were the $Ti_3C_2T_x$@PANI/SMPI-2, $Ti_3C_2T_x$@PANI/SMPI-4, $Ti_3C_2T_x$@PANI/SMPI-6, $Ti_3C_2T_x$@PANI/SMPI-8, $Ti_3C_2T_x$@PANI/SMPI-10, respectively.

improving the overall crystallinity of the $Ti_3C_2T_x$ @PANI/SMPI composites.

3.2. Microscopic topography

SEM-EDS was used to examine the morphology and etching quality of MXene. Fig. 3(a) shows etched accordion-like multilayer $Ti_3C_2T_x$. The etched MXene lamellae were smaller than 10 μm. The sheet edges were clean and smooth, with no obvious particle oxidation on or around the surface, indicating that the prepared MXene consisted of large sheets with few defects. EDS mapping revealed Ti, O, F, Cl, and C in the MXene, with negligible Al, confirming complete etching of the Al layer in Ti_3AlC_2 and the presence of surface polar groups such as −O, −F, and −Cl. The multilayer MXene was then ultrasonically exfoliated to obtain few-layer $Ti_3C_2T_x$, whose morphology and size were characterized by HRTEM and AFM. As shown in Fig. 3(b), the HRTEM image shows only a few lamellae, with thin, nearly transparent boundaries and distinct, tightly packed crystalline regions. These features suggested that MXene could act as a rigid layered microcrystalline component in the intercalation-complex reinforcement, thereby enhancing the mechanical strength of $Ti_3C_2T_x$@PANI/SMPI composites. AFM was used to measure the dimensions of the MXene sheets. As shown in Fig. 3(c), the lateral width was approximately 3.5 μm and the thickness was approximately 270 nm.

SEM was used to characterize the intercalation of $Ti_3C_2T_x$@PANI and its dispersion in the SMPI matrix. As shown in Fig. 3(d)-A, many fine micro/nanoscale particles were distributed on the surface and between the layers of the MXene sheets, indicating successful intercalation of PANI into the MXene lamellae. Fig. 3(d)-B ~ F show SEM images of $Ti_3C_2T_x$@PANI/SMPI composites containing 2, 4, 6, 8, and 10 wt% $Ti_3C_2T_x$@PANI. The MXene component was retained after imidization. $Ti_3C_2T_x$@PANI was well dispersed at moderate loadings (2–6 wt%), whereas partial aggregation occurred at higher loadings (8–10 wt%). The interface between the MXene lamellae and the resin matrix was strongly bonded, with almost no interfacial gaps. This strong interfacial adhesion can be attributed to Van Der Waals interactions and robust hydrogen bonding among the polyamic acid precursor, polyimide matrix, and MXene. Consequently, the polyimide acted as a binder, strengthening interactions between MXene sheets and improving interfacial adhesion.

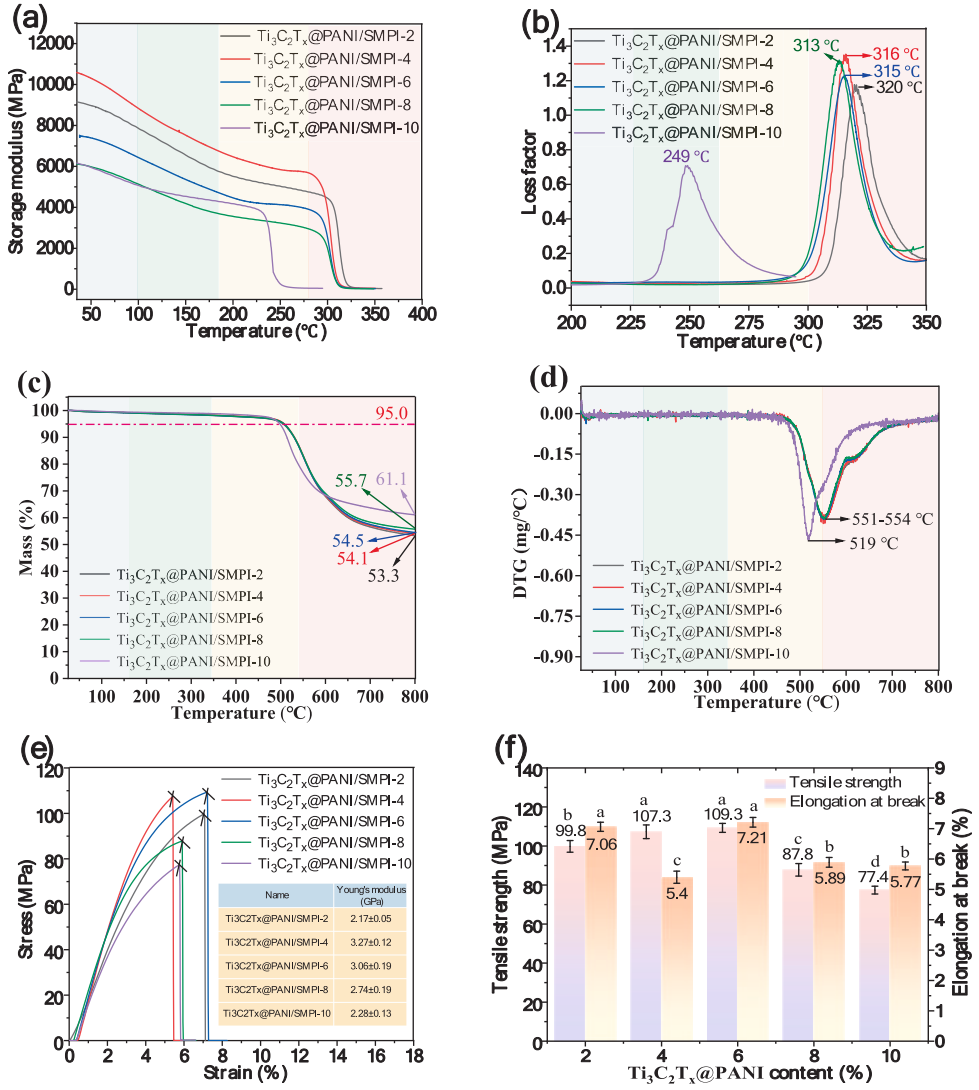

Fig. 4. (a) The storage modulus curves of $Ti_3C_2T_x$@PANI/SMPI composites, (b) The loss factor curves of $Ti_3C_2T_x$@PANI/SMPI composites, (c) The TGA curves of $Ti_3C_2T_x$@PANI/SMPI composites, (d) The DTG curves of $Ti_3C_2T_x$@PANI/SMPI composites, (e) The stress–strain curves and Young's modulus data of $Ti_3C_2T_x$@PANI/SMPI composites, respectively, (f) The mechanical properties data of $Ti_3C_2T_x$@PANI/SMPI composites.

3.3. Thermomechanical properties, mechanical properties and thermal stability

Fig. 4(a, b) were the storage modulus and loss factor curves of the $Ti_3C_2T_x$@PANI/SMPI composites, respectively. As shown in Fig. 4(a), the room temperature storage modulus first increased and then decreased with increasing filler content. $Ti_3C_2T_x$@PANI/SMPI-4 showed the highest storage modulus (10.5 GPa). As the temperature increased from 25 to 350 °C, the storage modulus continuously decreased. A broad transition step appeared between 240 and 320 °C, corresponding to the glass transition temperature (T_g). Within this region, the storage modulus decreased rapidly by approximately two orders of magnitude. This pronounced modulus change before and after glass transition is favorable for fixing temporary shapes in the composites.

In Fig. 4(b), the loss factor peaks of the $Ti_3C_2T_x$@PANI/SMPI composites were in the range of 249 °C − 320 °C. The temperature at which the loss factor peak occurred corresponds to the T_g. As summarized in Table 1 (Supporting Information, SI), $Ti_3C_2T_x$@PANI/SMPI-2 showed the highest T_g of 320 °C, whereas T_g gradually decreased with further $Ti_3C_2T_x$@PANI loading and reached 249 °C for $Ti_3C_2T_x$@PANI/SMPI-10. The low T_g of the 10 wt% sample is caused by competing effects at high filler loading. Although the rigid MXene/PANI interfaces can restrict part of the chains, excessive $Ti_3C_2T_x$@PANI is more likely to aggregate, disturb chain packing, and create heterogeneous, free-volume-rich interfacial regions. At the same time, the thermally conductive $Ti_3C_2T_x$@PANI network facilitates heat transfer through the composite, allowing local chain segments to reach their relaxation state at a lower measured temperature. These effects broaden the relaxation process and shift the loss factor peak to 249 °C for $Ti_3C_2T_x$@PANI/SMPI-10. Thus, the 10 wt% sample does not show a new matrix transition; rather, its lower T_g reflects high-filler-induced aggregation, interphase heterogeneity, and enhanced heat transport.

Fig. 4(c, d) show the TG and DTG curves of the $Ti_3C_2T_x$@PANI/SMPI composites, respectively. Fig. S1 (SI) show the TGA and DTG curves of PANI. In the DTG curves, the peak position corresponds to the temperature at which the material reaches its maximum decomposition rate, and a sharper or more intense peak indicates faster mass loss. For polymer materials, an initial mass loss of 0–5 % is usually associated with the volatilization of absorbed small molecules, residual monomers, or solvents. Therefore, the 5 % mass-loss temperature ($T_{dec,\ 5\ \%}$) is commonly used as the onset decomposition temperature. The residual mass at 800 °C reflects the char-forming ability and the amount of thermally stable inorganic residue remaining after decomposition and carbonization. Accordingly, the thermal stability of the composites was evaluated comprehensively using three parameters: $T_{dec,\ 5\ \%}$, the maximum decomposition-rate temperature ($T_{dec,\ max}$), and the residual mass at 800 °C (R_{800}). The TG and DTG results show that the $T_{dec,\ 5\ \%}$ values of the $Ti_3C_2T_x$@PANI/SMPI composites were in the range of 498–508 °C, indicating that the composites could remain stable below approximately 490 °C. Rapid decomposition of the polyimide chains occurred mainly between 510 and 700 °C, with $T_{dec,\ max}$ values of 519–554 °C. In addition, all composites retained more than 50 % residual mass at 800 °C. These high $T_{dec,\ 5\ \%}$, $T_{dec,\ max}$, and R_{800} values together demonstrate the excellent thermal stability of the SMPI composites. This stability is attributed to the abundant aromatic and heterocyclic structures in the polyimide chains, including benzene and imide rings, whose high bond energies and strong intermolecular interactions require high temperatures for bond cleavage.

The thermal-stability data for the PANI and $Ti_3C_2T_x$@PANI/SMPI composites are listed in Fig. S1 and Table 2 (SI). As the $Ti_3C_2T_x$@PANI content increased, R_{800} also increased because MXene was converted to TiO_2 at 800 °C. TiO_2 has a melting point of 1840 °C and a boiling point of 2900 °C and therefore remains stable at 800 °C. Besides, PANI has a residual mass of 36.8 % at 800 °C, which also makes a certain contribution to the total residue. Thus, a higher loading of the $Ti_3C_2T_x$@PANI led to a greater residual mass at 800 °C. Among the composite films, $Ti_3C_2T_x$@PANI/SMPI-10 showed the highest R_{800} value (61.1 %), but it also exhibited the lowest $T_{dec,\ 5\ \%}$ value (498 °C). In contrast, $Ti_3C_2T_x$@PANI/SMPI-2 had the lowest R_{800} value (53.3 %). These results indicate that the thermal stability should not be judged from the residual mass alone; instead, $T_{dec,\ 5\ \%}$, $T_{dec,\ max}$, and R_{800} should be considered together. Based on this combined evaluation, the composite films containing 4–8 wt% $Ti_3C_2T_x$@PANI exhibited the most balanced and optimal thermal stability.

Fig. 4(e, f) show the mechanical-property curves and statistical results for the $Ti_3C_2T_x$@PANI/SMPI composites. With increasing $Ti_3C_2T_x$@PANI content, both Young's modulus and tensile strength first increased and then decreased. $Ti_3C_2T_x$@PANI/SMPI-4 exhibited the highest Young's modulus (3.27 GPa) and a tensile strength of 107.3 MPa. $Ti_3C_2T_x$@PANI/SMPI-6 showed the highest tensile strength (109.3) MPa, while maintaining a Young's modulus of 3.06 GPa. The improved mechanical performance is mainly attributed to strengthened interfacial interactions and the reinforcing effect of the layered MXene/PANI structure. Hydrogen bonding between the polyimide matrix and the $Ti_3C_2T_x$@PANI intercalation complex enhanced the MXene/matrix interface and promoted stress transfer, allowing external loads to be distributed more uniformly throughout the SMPI film. In addition, the two-dimensional MXene sheets delayed microcrack initiation and propagation by dissipating load energy through crack bridging, crack pinning, crack deflection, interfacial sliding, and nanosheet pull-out. The elongation at break decreased from 7.06 % for $Ti_3C_2T_x$@PANI/SMPI-2 to 5.40 % for $Ti_3C_2T_x$@PANI/SMPI-4 because the rigid MXene/PANI domains and hydrogen-bonded interfaces restricted chain mobility. It then recovered to 7.21 % for $Ti_3C_2T_x$@PANI/SMPI-6, where a more developed layered network provided additional energy-dissipation pathways while maintaining high tensile strength. At higher loadings (8 and 10 wt%), however, excessive $Ti_3C_2T_x$@PANI disrupted chain packing and aggravated filler aggregation, creating defects, voids, and stress-concentration sites that facilitated crack formation during tensile loading and reduced both tensile strength and Young's modulus.

In addition, we performed statistical analysis among different filler contents and added significance markers to Fig. 4f. One-way ANOVA followed by Holm-adjusted Welch pairwise t-tests was used to evaluate significant differences among the groups, with $p < 0.05$ considered statistically significant. The significant differences have been marked in the revised figure using compact letter display. The results show that the 4 wt% $Ti_3C_2T_x$@PANI group exhibits significantly lower elongation at break than all other groups, which coincides with its peak Young's modulus (see Fig. 4e). This inverse trend suggests that at 4 wt% loading, the filler establishes the strongest interfacial interactions and physical crosslinking with the SMPI matrix, severely restricting chain slippage and orientation. Beyond 6 wt%, the modulus declines, indicating that filler agglomeration disrupts the rigid network and restores matrix deformability. Collectively, these findings confirm 4 wt% $Ti_3C_2T_x$@PANI as the critical threshold for the most compact interfacial bonding.

3.4. EMI shielding properties and extreme environmental resistance

Fig. 5(a-f) illustrate the EMI shielding performance of the $Ti_3C_2T_x$@PANI/SMPI composites over the frequency range of 8.2 to 12.4 GHz. At 2 wt% $Ti_3C_2T_x$@PANI/SMPI, the EMI *SE* was less than 5 dB. As the loading of the $Ti_3C_2T_x$@PANI increased, the EMI shielding performance progressively improved. When the $Ti_3C_2T_x$@PANI/SMPI content reached or exceeded 8 wt%, the composite film achieved an EMI *SE* exceeding 20 dB, meeting the requirement for commercial EMI shielding. According to the electromagnetic shielding efficiency equation: Shielding efficiency $= [1 - 1/(10^{SE/10})] \times 100\%$, more than 99 % of the incident microwaves can be effectively shielded. SE_R and SE_A represent the ability of the shielding material to attenuate electromagnetic waves entering the material, and both increased with $Ti_3C_2T_x$@PANI content. In the $Ti_3C_2T_x$@PANI/SMPI composite film, SE_A

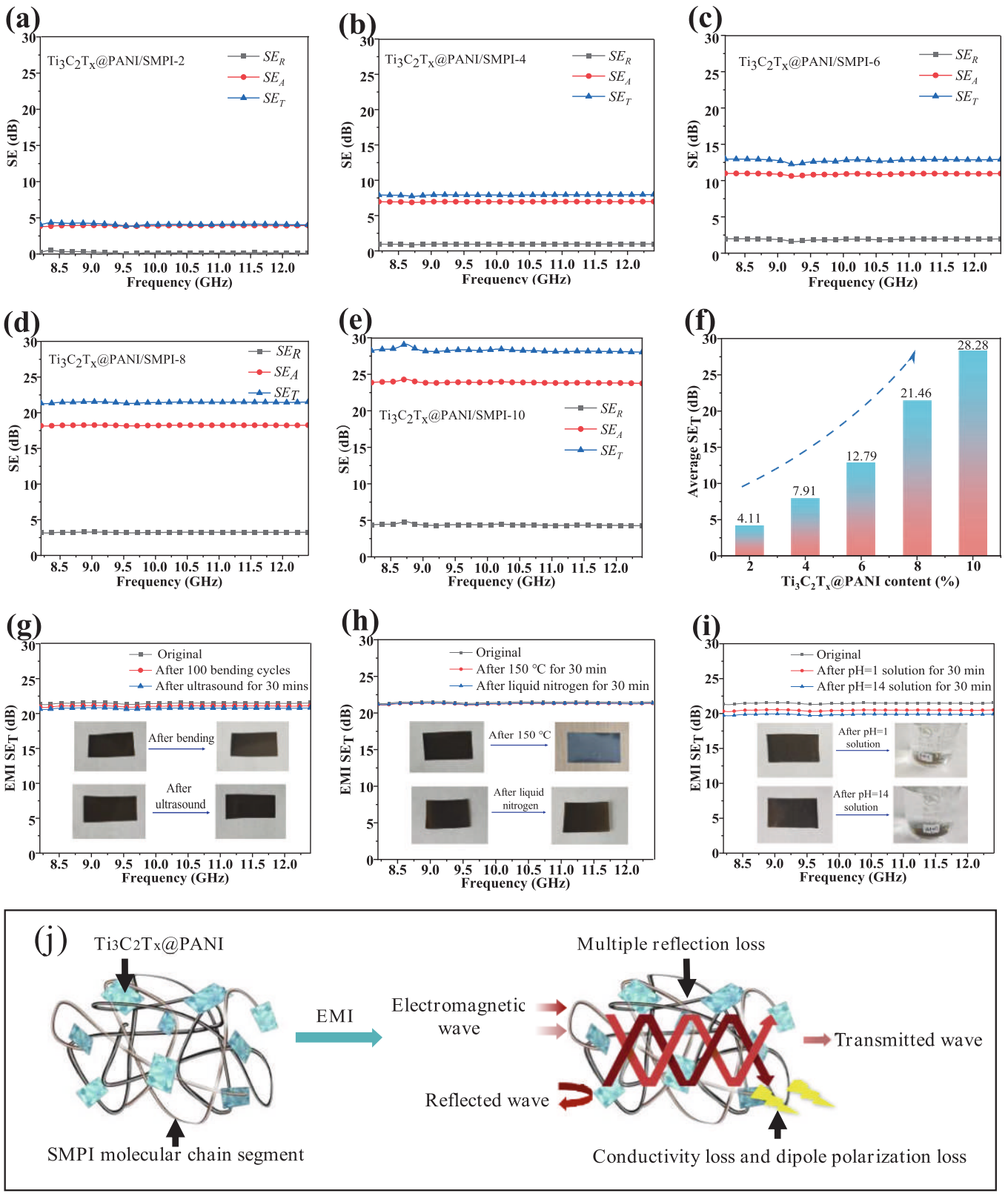

Fig. 5. (a-e) The EMI *SE* properties of $Ti_3C_2T_x$@PANI/SMPI composites films, among them, a-e were the $Ti_3C_2T_x$@PANI content of 2 wt%, 4 wt%, 6 wt%, 8 wt% and 10 wt%, respectively, (f) The average EMI SE_T of $Ti_3C_2T_x$@PANI/SMPI composites films, (g-i) Comparison of SE_T for $Ti_3C_2T_x$@PANI/SMPI-8 after 100 bending cycles and ultrasonication for 30 min, after exposure to 150℃ and liquid nitrogen environments for 30 min, and after exposure to salt solution and acidic environments for 30 min, (j) Schematic illustration of the electromagnetic shielding mechanism of $Ti_3C_2T_x$@PANI/SMPI composites.

contributed more than 75 % of SE_T, exceeding the contribution from SE_R. Therefore, the absorption mechanism plays a leading role in the $Ti_3C_2T_x$@PANI/SMPI composites, and secondary electromagnetic-wave pollution can be largely avoided in practical applications.

The EMI shielding stability of $Ti_3C_2T_x$@PANI/SMPI composite films under extreme environments is critical for practical applications. As shown in Fig. 5(g), after 100 bending cycles and 30 min of ultrasonic treatment, $Ti_3C_2T_x$@PANI/SMPI-8 retained good macroscopic structural integrity, flexibility, and stable EMI shielding performance, indicating robust mechanical durability. In addition, the *SE* curves in Fig. 5(h) after exposure to 150 °C and liquid nitrogen for 30 min were almost identical to those of the original samples, demonstrating excellent high- and low-temperature stability. As shown in Fig. 5(i), after immersion in 0.5 mol/L HCl and 0.5 mol/L NaOH solutions for 30 min, the composite maintained good macrostructural integrity. After drying, its EMI *SE* curves closely matched those of the original sample, demonstrating excellent acid and alkali resistance. This stability can be attributed to the tolerance of SMPI to extreme environments. The SMPI matrix encapsulated $Ti_3C_2T_x$@PANI and protected it effectively, thereby maintaining the EMI shielding stability of the composite film under harsh conditions.

The electromagnetic shielding mechanism is illustrated in Fig. 5(j). When electromagnetic waves strike the composite surface, abundant charge carriers on the $Ti_3C_2T_x$@PANI intercalation complex immediately reflect part of the incident waves. The remaining waves enter the material under the influence of induced dipoles generated by surface functional groups and are repeatedly scattered between layers until they are attenuated. The excellent electromagnetic-wave absorption of two-dimensional $Ti_3C_2T_x$ arises from its high conductivity, large specific surface area, abundant functional groups, and surface defects. Conductive PANI forms an intercalation complex with $Ti_3C_2T_x$ and further enhances the shielding effect of the $Ti_3C_2T_x$@PANI/SMPI composite. In addition, incorporation of $Ti_3C_2T_x$@PANI into the polyimide matrix creates numerous internal interfaces. Electromagnetic waves are attenuated through multiple scattering and interfacial polarization; consequently, absorption loss contributes more to the overall shielding effectiveness than reflection loss.

3.5. *Flame retardancy of the $Ti_3C_2T_x$@PANI/SMPI*

Flame retardancy describes a material's ability to delay flame spread. Plastic flame retardancy ratings increase in the order HB, V-2, V-1, and V-0. In this study, the flame retardancy grades of the $Ti_3C_2T_x$@PANI/SMPI composites were determined by the vertical burning method, and the results are shown in Table 3 (SI). All composites reached the V-0 rating. During testing, the composites showed no open-flame combustion or afterflame. Smoke generation was minimal and decreased with increasing $Ti_3C_2T_x$@PANI content, indicating that incorporation of two-dimensional MXene particles improved flame retardancy. In addition, the composites were self-extinguishing, showed no melt dripping, and did not ignite absorbent cotton. After combustion, the composites turned black; samples with higher $Ti_3C_2T_x$@PANI content showed more white deposits on their surfaces. To quantitatively evaluate flame retardancy, the limiting oxygen index (LOI) of the $Ti_3C_2T_x$@PANI/SMPI composites was measured. LOI evaluates the combustibility of materials in oxygen/nitrogen mixtures. A higher LOI indicates lower flammability, and materials with LOI values greater than 27 % are generally considered flame-retardant. As shown in Fig. 6(a), the LOI of the SMPI matrix resin was 29.4 %, confirming its intrinsic flame retardancy. The LOI of the composites increased continuously with increasing intercalation-complex content, and $Ti_3C_2T_x$@PANI/SMPI-10 showed the

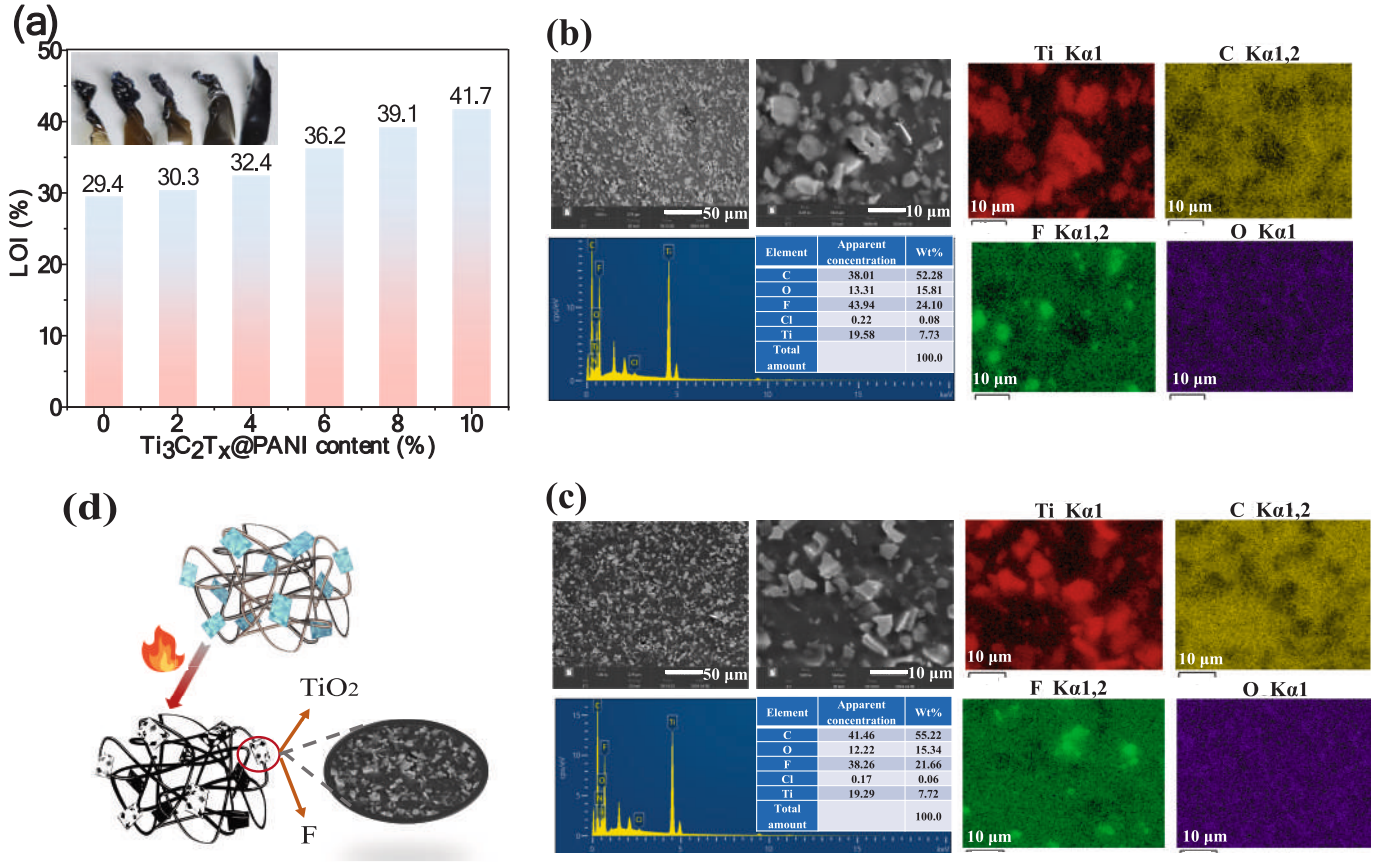

Fig. 6. (a) The LOI value of $Ti_3C_2T_x$@PANI/SMPI composites, and the upper left images were the composites after vertical combustion, among them, $Ti_3C_2T_x$@PANI content was 2 wt%, 4 wt%, 6 wt%, 8 wt%, and 10 wt% from left to right, (b) SEM-EDS images of $Ti_3C_2T_x$@PANI/SMPI-6 after combustion, (c) SEM-EDS images of $Ti_3C_2T_x$@PANI/SMPI-8 after combustion, (d) The diagram of the flame-retardant mechanism of $Ti_3C_2T_x$@PANI/SMPI composites.

highest LOI value (41.7 %). These results demonstrate that the composites can provide reliable flame protection for devices operating in high-temperature environments.

SEM-EDS was used to analyze the morphology and composition of $Ti_3C_2T_x$@PANI/SMPI-6 and $Ti_3C_2T_x$@PANI/SMPI-8 after combustion. As shown in Fig. 6(b, c), the MXene-sheet microstructure changed after burning, and the multilayer sheet structure was no longer visible. Instead, small TiO_2 particles and fragments were uniformly distributed on the SMPI film surface. Fig. 6(d) illustrates the proposed flame-retardant mechanism, in which the synergistic effect between MXene and SMPI endows the composite film with excellent flame retardancy. $Ti_3C_2T_x$ undergoes oxidation in air; upon heating, Ti-OH groups are gradually converted into Ti-O-Ti bonds, which further react with oxygen and water to form TiO_2 and carbon [33,34]. Consequently, increasing $Ti_3C_2T_x$@PANI content generates more TiO_2, resulting in more white deposits on the composite-film surface. The formed TiO_2 can act as a physical protective layer at the MXene-SMPI interface, encapsulating the carbonized SMPI residue and effectively suppressing combustion of the underlying material and further flame propagation. In addition, 4,4′-(hexafluoroisopropylidene)diphthalic anhydride and 4,4′-diaminodiphenyl ether were selected as monomers for SMPI synthesis to improve device safety; the fluorine-containing structure also contributes to flame retardancy.

3.6. Temperature-field-actuated deformation and adaptive electromagnetic-shielding devices

Fig. 7(a-c) show the shape memory behavior of $Ti_3C_2T_x$@PANI/SMPI-6 in "U" and "W" temporary shapes and after secondary folding. The "U" temporary shape fully recovered its original form after 8 s of thermal stimulation. The "W" temporary shape completely recovered after 12 s, and the secondary-folded temporary shape fully recovered after 15 s under the thermal field. Specifically, $Ti_3C_2T_x$@PANI/SMPI-6 was heated to 325 °C, formed into a "U" configuration under an applied

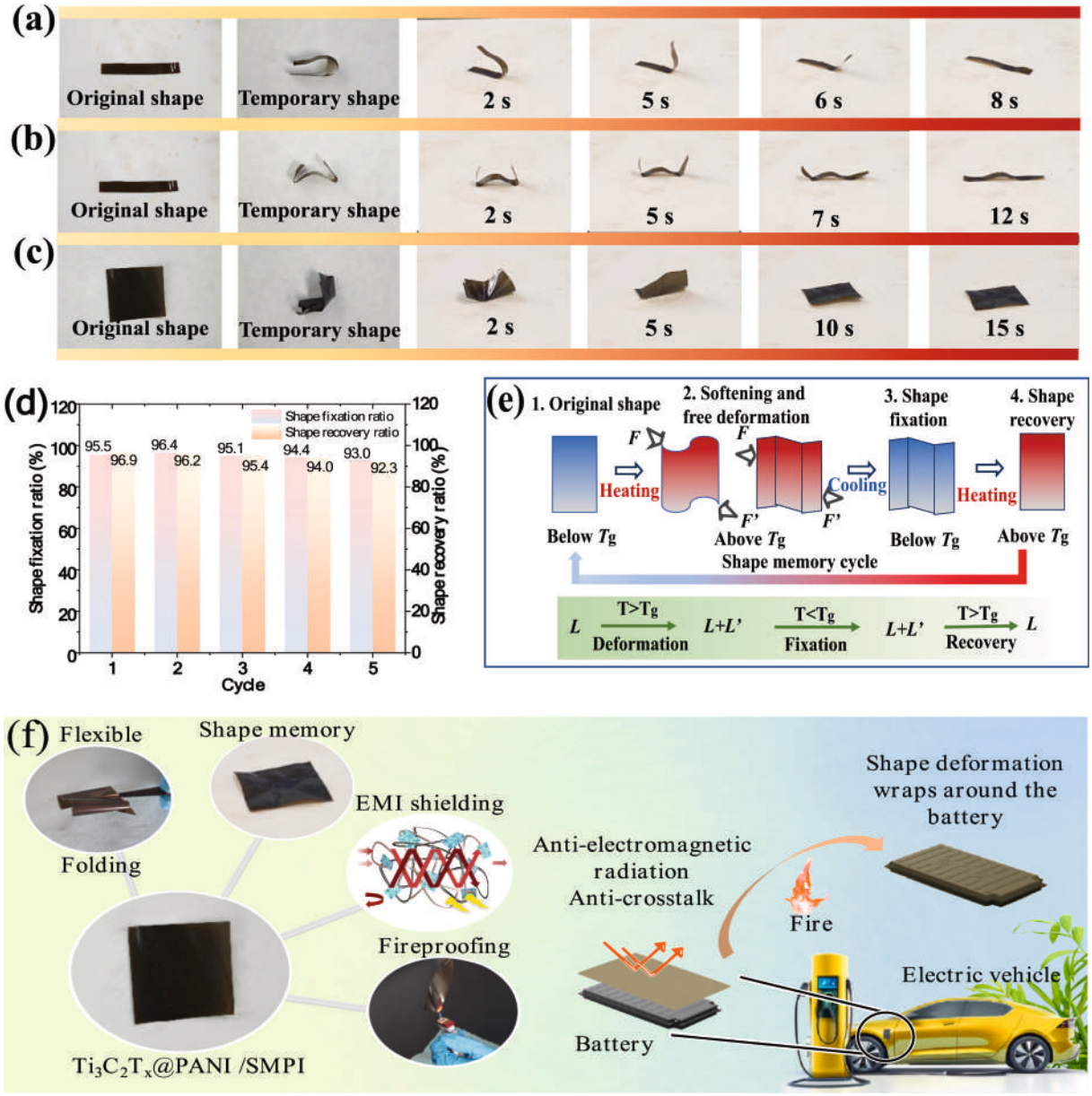

Fig. 7. The shape memory process of $Ti_3C_2T_x$@PANI/SMPI-6: (a) "U" shape, (b) "W" shape, (c) Secondary folding shape, (d) The results of five times shape memory cycles, (e) The diagram of shape memory mechanism, (f) Superior performance of $Ti_3C_2T_x$@PANI/SMPI composites and schematic of their future applications in new energy vehicles (NEVs).

load (radius of curvature R = 2.5 mm), and then cooled to room temperature. After cooling, the external force was removed, and the film retained its temporary "U" shape. When reheated to 325 °C, the film fully returned to its original shape within 8 s. This rapid recovery is mainly associated with the $Ti_3C_2T_x$@PANI particles. As a transition-metal carbide/nitride, $Ti_3C_2T_x$ has good thermal conductivity and can rapidly transfer heat from the thermal field to the resin matrix, thereby activating molecular chain segments from the frozen state. Fig. 7(d) shows the shape fixation and recovery ratios obtained from five DMA cycles. Both ratios remained above 90 %, confirming excellent shape memory performance. However, the shape memory performance gradually decreased with increasing cycle number, primarily because of permanent slippage of some molecular chain segments.

The proposed shape memory mechanism of the $Ti_3C_2T_x$@PANI/SMPI composite is schematically shown in Fig. 7(e). In principle, the shape memory effect of SMPI arises from molecular chain segments that form stationary and reversible phases through physical crosslinking. The stationary phase consists of physical crosslinking networks formed by π-π interactions between aromatic rings, hydrogen bonding, and molecular chain entanglement. The reversible phase consists of flexible chain segments such as ether bonds and $-CF_3$ groups. When the temperature exceeds T_g, the reversible phase softens while the stationary phase remains fixed. Molecular chain segments in the reversible phase become mobile and gradually reach thermodynamic equilibrium under the recovery stress provided by the stationary phase, which macroscopically appears as shape recovery.

The $Ti_3C_2T_x$@PANI/SMPI composite exhibits high EMI shielding performance and integrates multiple desirable functions, including excellent flexibility, shape memory effects, and flame retardancy, as illustrated in Fig. 7(f). Given these properties, it is envisioned that the composite could potentially serve as an EMI shielding patch for protecting internal components in applications such as robots, new energy vehicles (NEVs), and electronic appliances. In a future NEV battery module, if the battery temperature rises excessively and poses a fire hazard, the shape memory composite might deform and wrap around the battery, thereby providing a flame retardant barrier and enhancing safety. However, it should be emphasized that the present work focuses solely on material-level feasibility; device-level prototype demonstration has not yet been carried out. Nevertheless, the results suggest that $Ti_3C_2T_x$@PANI/SMPI composites hold promise for applications in adaptive deformation of advanced aircraft, electronic devices, thermal management electromagnetic shielding systems, and smart wearable electronics, pending further engineering development.

4. Conclusions

In this study, a high-temperature-resistant smart EMI-shielding composite was designed by coupling shape memory polyimide with a two-dimensional $Ti_3C_2T_x$@PANI intercalation complex. MXene sheets were etched to enrich their surfaces with –OH, =O, –F, and –Cl polar groups. Conductive PANI was then intercalated into MXene to obtain $Ti_3C_2T_x$@PANI intercalation complexes. The $Ti_3C_2T_x$@PANI/SMPI composite exhibited a tensile strength of 109.3 MPa, a storage modulus of 10.5 GPa, an initial decomposition temperature of 508 °C, a residual mass of 61.1 % at 800 °C, and a LOI of 41.7 %. In addition, its EMI shielding effectiveness in the X-band exceeded 28 dB, corresponding to attenuation of more than 99 % of incident microwaves, and the composite showed excellent extreme-environment resistance. It also exhibited excellent shape memory behavior, with a shape recovery ratio of 97 % and a shape fixation ratio of 96 %. These results demonstrate that the smart composites are promising for adaptive flame-retardant protective EMI-shielding devices and smart wearable devices.

CRediT authorship contribution statement

Xiaofei Wang: Writing – review & editing, Writing – original draft, Visualization, Methodology, Investigation, Data curation. **Ying Dai:** Writing – review & editing, Visualization, Data curation. **Shuting Jiang:** Writing – review & editing, Visualization, Data curation. **Xinli Xiao:** Supervision, Project administration, Data curation, Conceptualization. **Yanju Liu:** Writing – review & editing, Supervision, Funding acquisition. **Jinsong Leng:** Writing – review & editing, Supervision, Project administration, Funding acquisition, Conceptualization.

Declaration of competing interest

The authors declare that they have no known competing financial interests or personal relationships that could have appeared to influence the work reported in this paper.

Acknowledgements

This work was supported by the National Natural Science Foundation of China (92271206, 12502141), the Fundamental Research Funds for the Central Universities (XNJKKGYDJ2026022), and the National Key R&D Program of China (2022YFB3805700).

Appendix A. Supplementary data

Supplementary data to this article can be found online at https://doi.org/10.1016/j.compositesa.2026.110251.

Data availability

Data will be made available on request.

References

[1] Tan XX, He Y, Wang CH, Zhang Y, Wang WS, Li HY, et al. Hierarchical mxene/Fe_3O_4/cellulose nanofiber composites with layer-by-layer architecture for high-performance electromagnetic interference shielding. Compos Sci Technol 2025; 265:111136. https://doi.org/10.1016/j.compscitech.2025.111136.
[2] Lu YB, Xu Z, Sun SH, Du M, Guo ZH, Zuo M, et al. Interfacial distribution of PMMA-grafted $Ti_3C_2T_x$ in PC/PVDF engineering blends for long-term stable superior electromagnetic shielding performance. Compos Part A-Appl S 2026;204:109585. https://doi.org/10.1016/j.compositesa.2026.109585.
[3] Jiang K, Ji ZC, Zheng YC, Huang S, Wang M. Surface micro-arrays enhancing electromagnetic interference shielding of polydimethylsiloxane/multiwalled carbon nanotubes nanocomposites. Nano Res 2025;18:94907153. https://doi.org/10.26599/NR.2025.94907153.
[4] Isari AA, Ghaffarkhah A, Hashemi SA, Wuttke S, Arjmand M. Structural design for EMI shielding: from underlying mechanisms to common pitfalls. J Adv Mater 2024; 36:2310683. https://doi.org/10.1002/adma.202310683.
[5] Zhang P, Wang WJ, Luo XM, Meng X, Teng M, Han SS, et al. Enhancing thermal insulating and flame retardancy of electromagnetic shielding polyester-based nonwoven fabric. J ACS Appl Polym Mater 2024;6:10284–97. https://doi.org/10.1021/acsapm.4c01403.
[6] Hao MY, Zhang ZJ, Qian X, Wu Y, Li MY, Zhu CX, et al. Bifunctional polyimide-based graphite foam with integrated thermal conduction and electromagnetic shielding capabilities. Compos Sci Technol 2026;275:111478. https://doi.org/10.1016/j.compscitech.2025.111478.
[7] Niu LY, Ding P, Yuan Z, Jia X, Wang ZH, Xu JH, et al. Flexible and high-performance compressed graphene foam/PDMS composite films for Joule heating and electromagnetic interference shielding. J Mater Sci 2025;60: 10814–30. https://doi.org/10.1007/s10853-025-11087-y.
[8] Zhang XT, Jin GQ, Liu Y, Zhang MY, Li CJ, Zhang XL, et al. Insulating and flexible electromagnetic-shielding nanofiber composite film for direct wrapping on electronics even in harsh conditions. Adv Compos Hybrid Mater 2025;8:206. https://doi.org/10.1007/s42114-025-01272-7.
[9] Choi JR, Han JHY, Yu WR, Lee HJ, Cho SC, Jung BM, et al. Facile fabrication of ultrathin graphene/cellulose composites with efficient electromagnetic interference shielding by spray deposition. J Mater Lett 2023;341:134264. https://doi.org/10.1016/j.matlet.2023.134264.
[10] Bai Y, Ju JY, Pan YJ, Zhang BY, Yan YH, Fei GQ. Shape memory-driven intelligent composite film for infrared stealth and adjustable EMI shielding. Small 2025: e10825. https://doi.org/10.1002/smll.202510825.
[11] Wang SN, Cheng ZY, Yan Y, Yao JR, Liu YJ, Tao JQ, et al. Programmable electromagnetic switching in shape memory-driven liquid metal/polyimide/aramid nanofiber aerogels for intelligent wave management. Adv Funct Mater 2025:e21612. https://doi.org/10.1002/adfm.202521612.
[12] Li J, Liang ZH, Liu JJ, Yu C, Zhang XL, Kan QH. A thermo-viscoelastic constitutive model addressing the cyclic shape memory effect for thermo-induced shape

memory polymers. J Smart Mater Struct 2023;32:035030. https://doi.org/10.1088/1361-665X/acb676.
[13] Li JM, Lu XY, Zhang HMJ, He HN, Zhou MX, Yang XP, et al. Supramolecular network-modified pyrolytically recycled carbon fiber composites with recyclability, shape-memory effects, and flame retardation. Compos Sci Technol 2026;274:111450. https://doi.org/10.1016/j.compscitech.2025.111450.
[14] Zhou SW, Zhou DL, Gu RR, Ma CS, Yu CY, Qu DH. Mechanically interlocked [c2] daisy chain backbone enabling advanced shape-memory polymeric materials. J Nat Commun 2024;15:1690. https://doi.org/10.1038/s41467-024-45980-y.
[15] Ramezani M, Getya D, Gitsov I, Monroe MBB. Solvent-free synthesis of biostable segmented polyurethane shape memory polymers for biomedical applications. J Mater Chem B 2024;12:1217–31. https://doi.org/10.1039/d3tb02472e.
[16] Wang XF, He Y, Liu YJ, Leng JS. Advances in shape memory polymers: Remote actuation, multi-stimuli control, 4D printing and prospective applications. J Mater Sci Eng R 2022;151:100702. https://doi.org/10.1016/j.mser.2022.100702.
[17] Li HY, Yang JH, Wang N, Yao L. Effect of stacking sequence on the electromagnetic shielding and mechanical properties of jute/graphite reinforced polylactic acid composites. Compos Part A-Appl S 2026;203:109550. https://doi.org/10.1016/j.compositesa.2025.109550.
[18] Wang XF, He Y, Xiao XL, Zhao W, Leng JS. High-T_g shape memory polyimide composites with "spot-plane" directional thermally conduction structure based on AlN nanoparticles and acidified graphene. Compos Struct 2024;330:117846. https://doi.org/10.1016/j.compstruct.2023.117846.
[19] Gholami R, Lawan I, Luengrojanakul P, Ebrahimi S, Ahn CH, Rimdusit S. Development of a laser induced graphene (LIG) and polylactic acid (PLA) shape memory polymer composite with simultaneous multi-stimuli response and deformation self-sensing characteristics. J Nanoscale Adv 2024;6:4865–76. https://doi.org/10.1039/d4na00450g.
[20] Wang XF, He Y, Leng JS. Shape memory polyimides and composites with tunable chain stiffness and ultrahigh transition temperature range. J Compos Part A-Appl Sci Manuf 2022;163:107237. https://doi.org/10.1016/j.compositesa.2022.107237.
[21] Liu Y, Wang YD, Wu N, Han MR, Liu W, Liu JR, et al. Diverse structural design strategies of MXene-based macrostructure for high-performance electromagnetic interference shielding. J Nano-Micro Lett 2023;15:240. https://doi.org/10.1007/s40820-023-01203-5.
[22] Wang L, Yang ZL, Lang L, Men JY, Gao TT, Wang Q, et al. Flexible multifunctional MXene/polyimide films with Janus structure for superior electromagnetic interference shielding. Adv Compos Hybrid Mater 2025;8:26. https://doi.org/10.1007/s42114-024-01100-4.
[23] Wang SW, Ma HY, Ge SB, Rezakazemi M, Han JQ. Advanced design strategies and multifunctional applications of Nanocellulose/MXene composites: a comprehensive review. Mater Sci Eng R 2025;163:100925. https://doi.org/10.1016/j.mser.2025.100925.
[24] Aghvami-Panah M, Ameli A. MXene/Cellulose composites as electromagnetic interference shields: Relationships between microstructural design and shielding performance. J Compos Part A-Appl Sci Manuf 2024;176:107879. https://doi.org/10.1016/j.compositesa.2023.107879.
[25] Kabir L, Qi JH, Wijaya K, Sagadevan S, Yoon CM, Ullah K, et al. Recent advances and latest technologies in energy storage applications based on 2D MXene. J Energy Storage 2024;80:110335. https://doi.org/10.1016/j.est.2023.110335.
[26] Duan J, Liu Z, Wang XC. Enhanced electromagnetic shielding and absorption in $Ti_3C_2T_x$ MXene films via hydroxyl functionalization and interlayer spacing control. Surf Coat Tech 2025;513:132503. https://doi.org/10.1016/j.surfcoat.2025.132503.
[27] Yan YZ, Chen K, Moon HR, Park SS, Ha CS. Flexible and hydrophobic polyimide/MXene-POSS nanocomposite films for electromagnetic interference shielding. J Eur Polym J 2024;202:112655. https://doi.org/10.1016/j.eurpolymj.2023.112655.
[28] Gu YQ, Yu LZ, Mou JG, Wu DH, Zhou PJ, Xu MS. Mechanical properties and application analysis of spider silk bionic material. J E-Polymers 2020;20:443–57. https://doi.org/10.1515/epoly-2020-0049.
[29] Wu SJ, Liu Z, Gong CH, Li WJ, Xu SJ, Wen R, et al. Spider-silk-inspired strong and tough hydrogel fibers with anti-freezing and water retention properties. Nature Communications, J Nat Commun 2024;15:4441. https://doi.org/10.1038/s41467-024-48745-9.
[30] Su YP, Shi S, Wang C, Wang Z, Li PS, Zhang ST, et al. Spider silk-inspired tough materials: Multi-pathway synthesis, advanced processing, and functional applications. J Nano Today 2024;55:102188. https://doi.org/10.1016/j.nantod.2024.102188.
[31] Song YH, Li JL, Song GJ, Li ZJ, Yang XR, Ma FL, et al. Superior strength, highly stretchable, bionic self-healing polyurethane and its composites for flexible conductivity and self-cleaning applications. J Compos Part B-Eng 2024;280:111457. https://doi.org/10.1016/j.compositesb.2024.111457.
[32] Li JJ, Chen YN, Zhang FD, Lyu Y, Li XN, Li K, et al. Spider silk-inspired high-performance soybean meal-based adhesive reinforced by greenly produced chitosan-functionalized boron nitride nanosheets. J Chem Eng 2022;438:135442. https://doi.org/10.1016/j.cej.2022.135442.
[33] Karlsson LH, Birch J, Halim J, Barsoum MW, Persson POÅ. Atomically resolved structural and chemical investigation of single MXene sheets. J Nano Lett 2015;15:4955–60. https://doi.org/10.1021/acs.nanolett.5b00737.
[34] Zhang CJ, Pinilla S, McEvoy N, Cullen CP, Anasori B, Long E, et al. Oxidation stability of colloidal two-dimensional titanium carbides (MXenes). J Chem Mater 2017;29:4848–56. https://doi.org/10.1021/acs.chemmater.7b00745.